

43 lubricates the ice/bed interface or saturates any sediment till layer, allowing higher ice
44 velocities via basal sliding. For instance, the rapid retreat of Thwaites and Pope glaciers
45 in the Amundsen Sea sector of West Antarctica is being facilitated by high heat flow in
46 the underlying lithosphere (Dziadek et al., 2021). This bed-ice linkage forms the basis
47 for making inferences on basal conditions via surface observations (Pattyn, 2010), or
48 relict landforms (e.g. Näslund et al., 2005).

49

50 The ice temperature is controlled by deformational heat generated from strain within
51 the ice, advection of heat due to lateral ice motion and the descent rate of ice from the
52 surface, conduction of heat through the ice and frictional heating from basal sliding. Ice
53 temperature is hard to evaluate because of the scarcity of in-situ measurements,
54 typically obtained from boreholes that are very rarely drilled through the Antarctic ice
55 sheet. GHF is an important boundary condition for ice temperature simulation, and is
56 generally the largest source of uncertainty. Hence geophysical survey methods are used
57 to indirectly map GHF. To date GHF datasets have been estimated from seismic models
58 (Shapiro and Ritzwoller, 2004; An et al., 2015; Shen et al., 2020), derived from airborne
59 magnetic surveys (Li et al., 2021; Martos et al., 2017) and satellite geomagnetic data
60 (Maule et al., 2005; Purucker, 2013).

61

62 Extensive ice penetrating radar data has been collected recently over Princess Elizabeth
63 Land (PEL; Fig. 1d), including the eastern part of the Lambert-Amery system (Cui et
64 al., 2020a). This fills in large data gaps from older surveys, and provides the basis for
65 our study. The radar surveys reveal ~1100 km long canyons (Fig. 1c) that are incised
66 hundreds of meters deep into the subglacial bed that extend from the Gamburtsev
67 Subglacial Mountains (GSM) to the coast of the Western Ice Shelf (WIS). Li et al. (2021)
68 collected airborne magnetic data that can be combined with radar ice thicknesses and
69 estimated depths at which the bedrock reaches its Curie temperature, to invert for the
70 geothermal flux. The resulting higher resolution data set (Li et al., 2021) implies a larger
71 heat flux than previous estimates in this region. Furthermore, recently discovered
72 subglacial lakes, including potentially the second largest subglacial lake in Antarctica,
73 add evidence for more widespread basal melting in the region than was thought based
74 on the much sparser earlier survey data (Cui et al., 2020b). The complex subglacial
75 topography, relatively high geothermal heat flux and subglacial lakes imply a complex
76 distribution of basal thermal conditions and subglacial water networks. These
77 heterogenous basal conditions will have shaped much of the ice flow and mass balance
78 of the Lambert-Amery system. This motivates us to investigate how the basal thermal
79 conditions inferred from the new high-resolution topography dataset can be reconciled
80 with surface ice velocities and existing geothermal heat flow maps.

81

82 Ice sheet models can be used to simulate the dynamics and thermodynamics of the ice
83 sheet. Glaciologists have combined ice sheet models with measurements of vertical
84 temperature profiles or thawed basal states to constrain GHF of the ice sheets (e.g.
85 Pattyn, 2010; Rezvanbehbahani et al., 2019). In the Lambert-Amery glacial system,
86 Pittard et al. (2016) suggest that ice flow is most sensitive to the spatial variation in the

87 underlying GHF near the ice divides and along the edges of the ice streams.

88

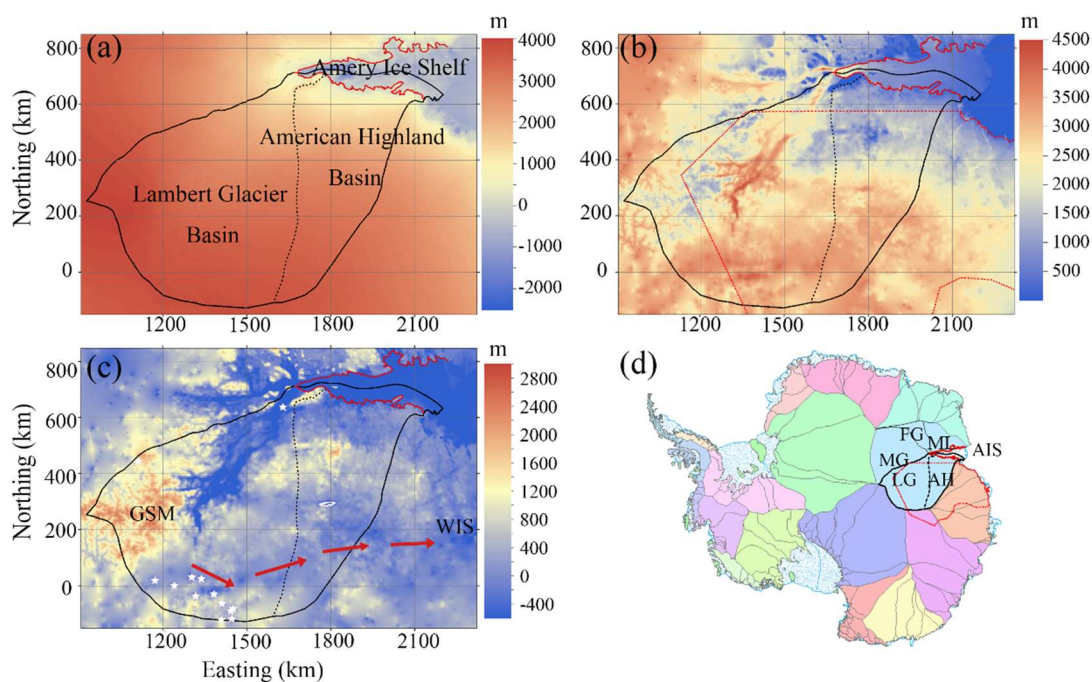
89 In this study, we simulate ice basal temperatures and basal melt rates in the Lambert-
90 Amery system using the new high-resolution digital elevation model, along with six
91 different published GHF maps as forcing for an off-line coupling between a basal
92 energy and water flow model and a 3D full-Stokes ice flow model. We evaluate the
93 quality of the resulting basal temperature field incorporating the Stokes model estimates
94 of ice advection, strain and frictional heating under the different GHF maps using all
95 available observed subglacial lakes and surface velocities. Hence, we make inferences
96 on which GHF maps yield the best match with observations in the region.

97

98 **2 Regional Domain and Datasets**

99 Our modeled domain is part of the Lambert-Amery system. It consists of two drainage
100 basins: the Lambert Glacier Basin, the American Highland Basin, along with about half
101 of the Amery Ice Shelf (Fig. 1). The 2D domain boundary outlines are defined by the
102 inland ice catchment basin boundary, the central streamline, and the ice front of Amery
103 Ice Shelf. The central streamline was chosen by selecting a point at the confluence of
104 Lambert Glacier and Lepekhin Glacier and then advecting that point downstream to the
105 ice front using the observed velocity field. The inland sub-basin and the central
106 streamline of the Amery Ice Shelf were chosen as boundaries because the mass flux
107 across them is assumed to be zero by definition.

108



109

110 Fig. 1. The domain topography and location with domain boundary overlain. (a) surface elevation;
111 (b) ice thickness; (c) bed elevation; (d) the location of our domain in Antarctica. The solid black
112 curve is the outline of the study domain, including the central streamline of Amery ice shelf and the
113 boundary of inland sub-basins based on drainage-basin boundaries defined from satellite ice sheet
114 surface elevation and velocities (Mouginot et al., 2017; Rignot et al., 2019). The solid red curve is

115 the grounding line of Amery ice shelf (Morlighem et al., 2020). The dotted black curve is the
 116 dividing line between Lambert Glacier Basin and the American Highland Basin. The dotted red
 117 curves in (b) and (d) are the boundary of ice thickness data from Cui et al. (2020a), inside which we
 118 incorporates data from Cui et al. (2020a). The white stars in (c) denote the locations of observed
 119 subglacial lakes (Wright and Siegert, 2012; Cui et al., 2021), and the region within the white line at
 120 (1800E, 300N) is potentially the second largest subglacial lake in Antarctic. The red arrows in (c)
 121 indicate the routing through the deep subglacial canyon system from GSM to WIS. The sub-basins
 122 names of Lambert-Amery system are labeled in (d), ML for MacRobertson Land basin, FG for
 123 Fisher glacier basin, MG for Mellor glacier basin, LG for Lambert glacier basin, AH for American
 124 Highland basin, and AIS for Amery Ice Shelf.

125
 126 The surface elevation, bedrock elevation, and ice thickness from Cui et al. (2020a) are
 127 used in most of the domain (Fig. 1b; Table 1) with additional data are from MEaSURES
 128 BedMachine Antarctica, version 2 at a resolution of 500 m (Morlighem et al., 2020).
 129 The bed elevation is calculated by subtraction of the ice thickness from the surface
 130 elevation.

131
 132 The surface ice velocity data are obtained from MEaSURES InSAR-based Antarctic ice
 133 velocity Map, version 2 with resolution of 450 m (Rignot et al., 2017). Data were largely
 134 acquired during the International Polar Years 2007 to 2009, and between 2013 and 2016.
 135 Additional data acquired between 1996 and 2016 were used as needed to maximize
 136 coverage.

137
 138 Ice sheet surface temperature data are prescribed by ALBMAP v1 with a resolution of
 139 5 km (Le Brocq et al., 2010) and come from monthly estimates inferred from AVHRR
 140 data averaged over 1982-2004. Subglacial lake locations are from the fourth inventory
 141 of Antarctic subglacial lakes (Wright and Siegert, 2012), with the addition of the newly
 142 discovered lakes (Cui et al., 2020b).

143
 144 Six GHF datasets (Fig. 2; Table 2) are used in this study. All the datasets are interpolated
 145 into the same 2.5 km resolution.

146
 147 Table 1 Datasets used in this study.

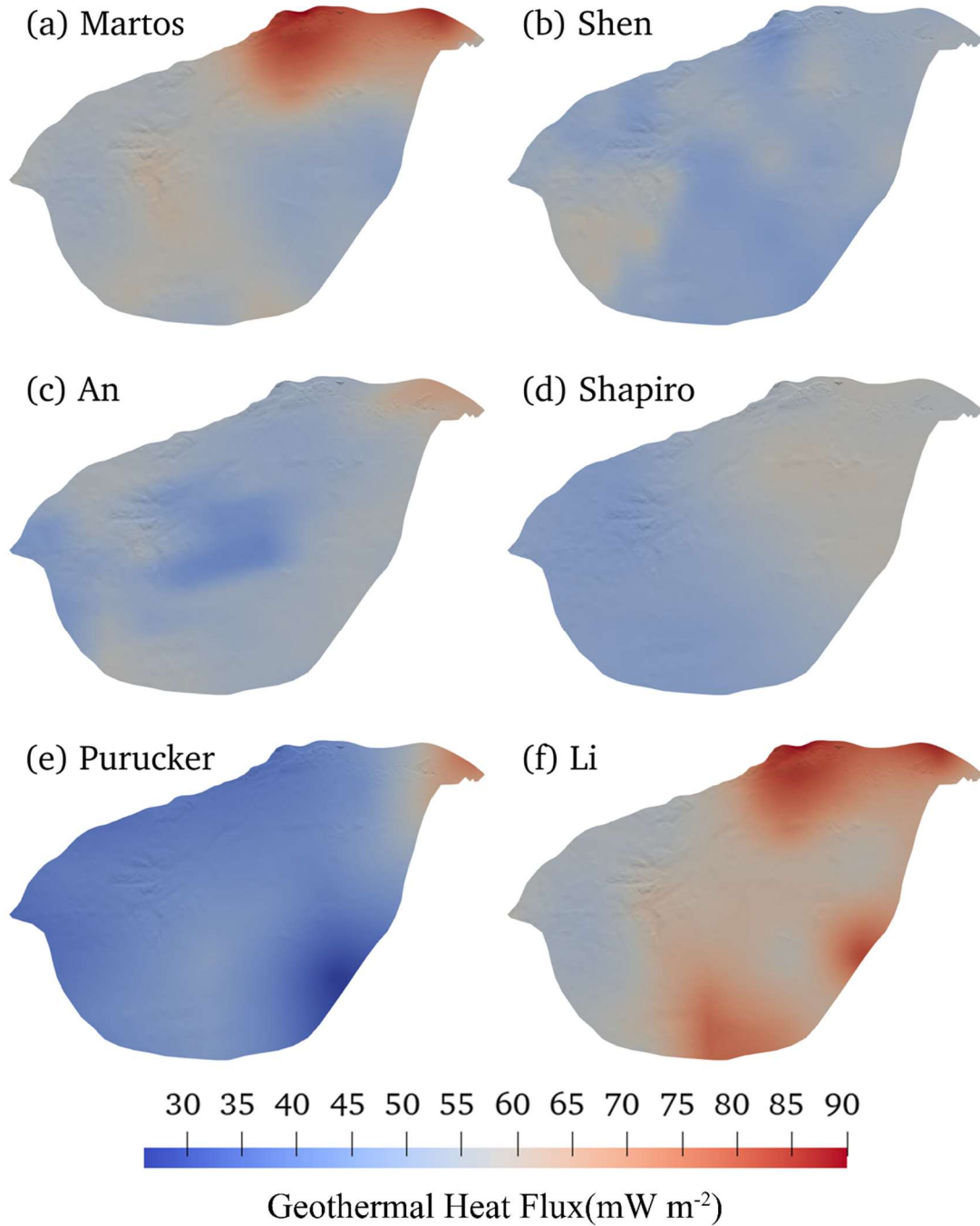
Variable name	Dataset	Resolution	Reference
surface elevation, bedrock elevation, and ice thickness	MEaSURES BedMachine Antarctica version 2	500 m	Morlighem et al., 2020; Cui et al., 2020
surface ice velocity	MEaSURES InSAR-based Antarctic ice velocity Map, version 2	450 m	Rignot et al., 2017
surface temperature	ALBMAP v1	5 km	Le Brocq et al., 2010;
subglacial lakes location	The fourth inventory of Antarctic subglacial lakes	-----	Wright and Siegert, 2012; Cui et al., 2021

148
 149 Table 2 The six GHF datasets used in this study.

GHF map	Reference	Method	Mean (mW m ⁻²)	Range (mW m ⁻²)
Martos	Martos et al., 2017	airborne geomagnetic data	72	47-90
Shen	Shen et al., 2020	seismic model	50	43-59
An	An et al., 2015	seismic model	55	40-66

Shapiro	Shapiro and Ritzwoller, 2004	seismic model	54	45-58
Purucker	Purucker, 2013	Satellite geomagnetic data	47	26-47
Li	Li et al., 2021	airborne geomagnetic data	72	52-90

150



151

152 Fig. 2. The spatial distribution of GHF over our domain as described in Fig. 1. See Table 2 for the
 153 GHF map details.

154

155 **3 Model**

156 Our goal is to infer the basal thermal conditions, including basal temperature and basal
157 melt rate in the domain. Geothermal heat flux, englacial heat conduction and basal
158 friction heat are the main heat sources that determine the basal thermal conditions.
159 Therefore, we need to model both ice flow velocity and stress for basal friction heat and
160 ice temperature for englacial heat conduction.

161

162 We solve an inverse problem by a full-Stokes model, implemented in Elmer/Ice, to infer
163 the basal friction coefficient such that the modelled velocity best fits observations
164 (Gagliardini et al., 2013). Using the best-fit basal friction coefficient, we obtain the ice
165 flow velocity, stress and basal friction heat. A proper initial ice temperature is needed
166 in solving the inverse problem. To get it, we use a forward model that consists of an
167 improved Shallow Ice Approximation (SIA) thermomechanical model with a
168 subglacial hydrology model (Wolovick et al., 2021a). The forward model uses the
169 modelled velocity direction and basal slip ratio from the full-Stokes inverse model to
170 constrain its solution. We do steady state simulations by coupling the two models. We
171 will describe the forward model in Section 3.1 and the inverse model in Section 3.2,
172 then the coupling in Section 3.3.

173 **3.1 Forward Model**

174 The forward model consists of a thermomechanical steady state model using an
175 improved Shallow Ice Approximation (SIA) in equilibrium with the subglacial
176 hydrological system (Wolovick et al., 2021a). It has internal consistency between three
177 components: ice flow, ice temperature, and basal water flux. The numerical model
178 requires three coupled components to be consistent with one another: (1) integration for
179 balance flux and englacial temperature downhill in the ice surface, (2) integration for
180 basal water flux and freezing rate downhill in the hydraulic potential, and (3) rheology
181 and shape function computations to determine the distribution of ice flux and shear
182 heating. The model performs a fixed-point iteration for consistency between these three
183 components. In addition, we improve on the model used in Wolovick et al. (2021a) by
184 combining the observed velocity field, the velocity field from the full-Stokes model,
185 and the surface gradient direction to compute a merged flow direction field for step (1).
186 The observations are used where flow is fast, Elmer/Ice modelled velocity is used where
187 flow is slow, and the surface gradient is only used near the margins of the domain where
188 the Elmer velocity field is not reliable (Fig. 3). The simulation is done on a finite
189 difference mesh with resolution of 2.5 km.

190

191 The surface accumulation rate we used in the forward thermal model is the mean of
192 Arthern et al. (2006) and Van de Berg et al. (2005). Both were accessed through the
193 ALBMAP_v1 dataset (Le Brocq et al., 2010).

194

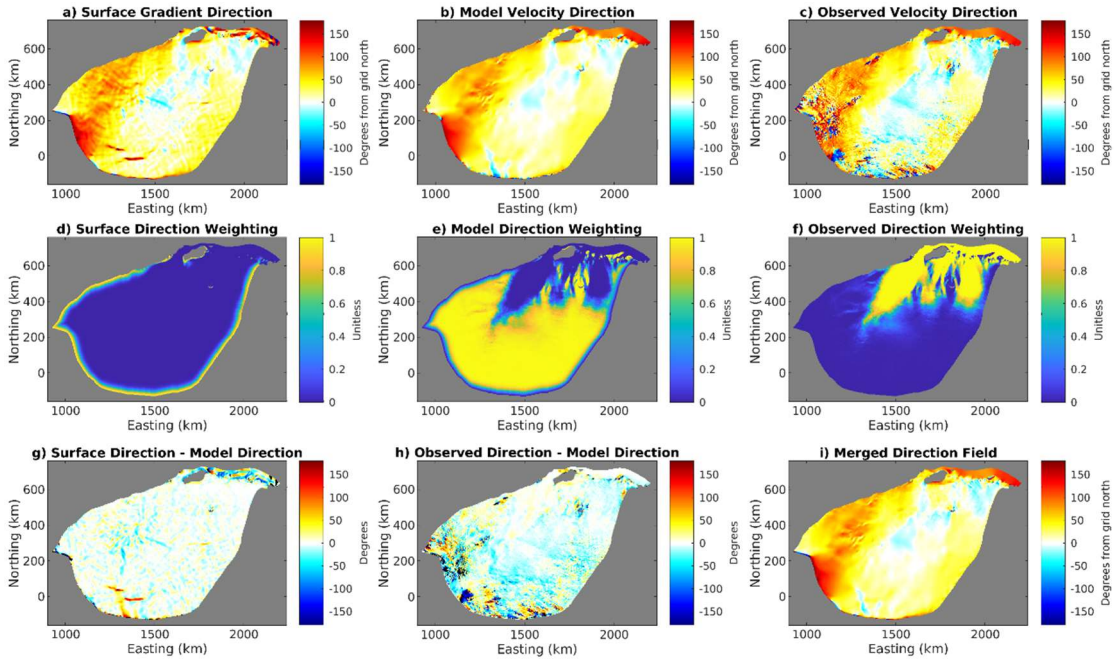
195 One key complexity is how to deal with basal thermal boundary condition. At the
196 bottom of ice shelves, we set basal temperature equal to the pressure melting point. At

197 the bed of grounded ice, the boundary condition can be either Dirichlet or Neumann
 198 condition depending on the basal melting and subglacial water conditions. The basal
 199 boundary conditions are given by,

$$200 \quad -k(T) \frac{dT}{dz} = G, \quad \text{for } T < T_m \text{ and } m = 0; \quad (1)$$

$$201 \quad T = T_m, \quad \text{for } m \neq 0, \quad (2)$$

202 where T_m is the pressure-dependent melting temperature, G is GHF, taking six GHF
 203 datasets listed in Table 2. The thermal condition will switch from Neumann (Eq 1) to
 204 Dirichlet (Eq 2) if the basal temperature exceeds the pressure-dependent melting point.
 205 The opposite switch from Dirichlet to Neumann is determined by the hydrology model,
 206 if there is insufficient water input to supply a large freezing rate.
 207



208
 209 Fig. 3. Velocity direction fields, in degrees clockwise from grid north. The first row shows the
 210 direction from surface gradient (a), Elmer/Ice modelled velocity (b), and the observed velocity
 211 direction (c). The middle row (d-f) shows the 3 corresponding weighting fields (the sum of these
 212 weights is 1). The bottom row shows the difference between the direction of surface gradient and
 213 Elmer/Ice modelled velocity (g), the difference between the observed velocity direction and
 214 Elmer/Ice modelled velocity (h), and the merged velocity field used in the forward model (i).

215 One improvement on the method from Wolovick et al. (2021a) is that a temperate basal
 216 ice layer with non-zero thickness is permitted in our model in the case that the modelled
 217 basal ice temperature reaches the pressure melting point. We do this using a weak-form
 218 solution in which the volumetric englacial melt rate rises steeply as temperature exceeds
 219 the melting point. The englacial melting absorbs latent heat and serves to limit
 220 temperature rise. We parameterize the increase in volumetric melt rate as an
 221 exponential function of temperature with a 1 K e-folding temperature, and a prefactor
 222 given by the englacial strain heating and the latent heat of fusion. All englacial
 223 meltwater generated this way is assumed to immediately drain to the bed.

224

225 Another key component of the forward model is the shape function determining the
226 distribution of horizontal velocity with depth. We also improve the shape function in
227 Wolovick et al. (2021a) by adding basal slip ratio, $\hat{u}_b = u_b/\bar{u}$, where u_b is the basal
228 velocity magnitude and \bar{u} is the vertically averaged horizontal velocity magnitude. The
229 slip ratio is taken from the full-Stokes inverse model. Other than the addition of a
230 spatially variable slip ratio, the shape function calculation is unchanged from Wolovick
231 et al. (2021a).

232 3.2 Inverse Model with full-Stokes Model

233 The spatial distribution of basal friction in the domain is modelled by solving an inverse
234 problem using the three-dimensional the full-Stokes model, Elmer/Ice, an open source
235 finite element method package(Gagliardini et al., 2013). The inverse model is based on
236 adjusting the spatial distribution of the basal friction coefficient to minimize the misfit
237 between simulated and observed surface velocities. The modelled velocity is obtained
238 by solving the full-Stokes equation, which includes conservation equations for both the
239 momentum and mass of the ice,

$$240 \quad \text{div } \boldsymbol{\tau} - \text{grad} p = \rho_i \vec{g}, \quad (3)$$

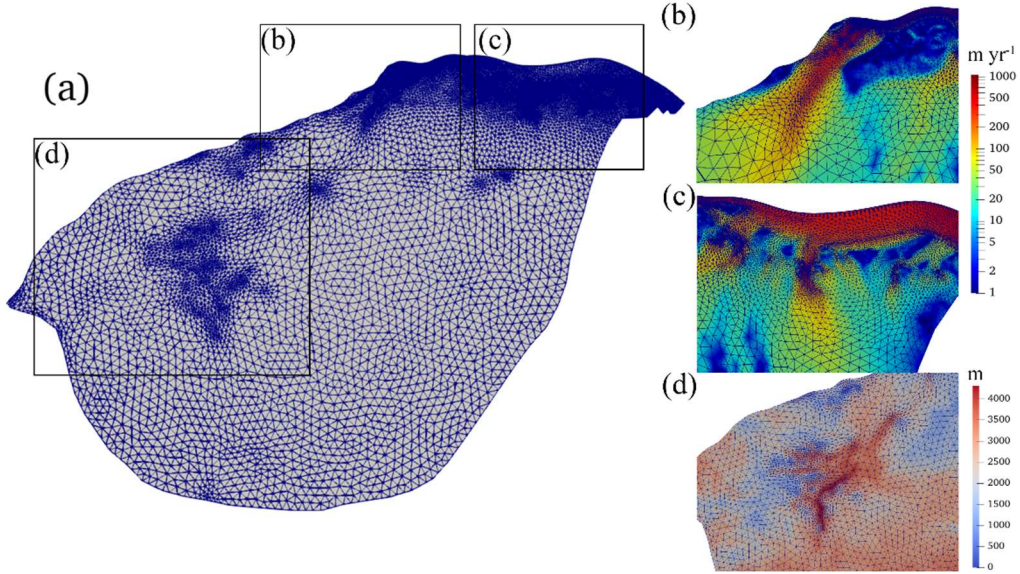
$$241 \quad \text{div } \vec{v} = 0, \quad (4)$$

242 where $\boldsymbol{\tau}$ is the deviatoric stress tensor, p is the isotropic pressure, ρ_i is ice density, \vec{g} is
243 the acceleration due to gravity $(0, 0, -9.81) \text{ m}\cdot\text{s}^{-2}$, \vec{v} is ice velocity. According to Glen's
244 flow relation, deviatoric stress is related to the deviatoric part of the strain rate tensor,
245 $\dot{\boldsymbol{\epsilon}}_E$, which can be described by $\boldsymbol{\tau} = 2\eta\dot{\boldsymbol{\epsilon}}_E$, where the effective viscosity of the ice, η , is
246 sensitive to the temperature-dependent flow rate factor $A(T)$ calculated using an
247 Arrhenius equation (Cuffey and Paterson, 2010). The ice temperature distribution
248 comes from the forward model in section 3.1.

249

250 3.2.1 Mesh Generation and Refinement

251 Firstly, we use GMSH (Geuzaine and Remacle, 2009) to generate an initial 2-D
252 horizontal footprint mesh with the boundary described in section 2. Then we refine the
253 mesh by an anisotropic mesh adaptation code called the Mmg library
254 (<http://www.mmgtools.org/>). The resulting mesh is shown in Fig. 4 and has minimum
255 and maximum element sizes of approximately 1000 m and 8000 m. The 2-D mesh is
256 then vertically extruded using 10 equally spaced, terrain following layers.



257
 258 Fig. 4. The refined 2-D horizontal domain footprint mesh (a). Boxes outlined in (a) are shown in
 259 detail overlain with surface ice velocity in (b) and (c), and with ice thickness in (d).
 260

261 3.2.2 Boundary Condition

262 The ice surface is assumed to be stress-free. At the ice front, the normal stress under the
 263 sea surface is equal to the hydrostatic water pressure. On the lateral boundary, the
 264 normal stress is equal to the ice pressure applied by neighboring glaciers and the normal
 265 velocity is assumed to be 0. The bed for grounded ice is assumed to be rigid,
 266 impenetrable, and fixed over time. Since we perform a stress-balance snapshot in the
 267 full-Stokes model, we do not need to prescribe surface mass balance or basal mass
 268 balance in the boundary conditions.

269
 270 The normal basal velocity is set to 0 at the ice-bed interface. The linear sliding law is
 271 used to describes the relationship between the basal sliding velocity, \vec{u}_b , and the basal
 272 shear force, $\vec{\tau}_b$, on the bottom of grounded ice,

$$273 \quad \vec{\tau}_b = C \vec{u}_b. \quad (5)$$

274 To avoid non-physical negative values, $C = 10^\beta$ is used in the simulation. We call β
 275 the basal friction coefficient rather than C . C is initialized to a constant value of 10^{-4}
 276 MPa m⁻¹ yr (Gillet-Chaulet et al., 2012), and then replaced with the inverted C in
 277 subsequent inversion steps.

279 3.2.3 Surface Relaxation

280 We relax the free surface of the domain by a short transient run to reduce the non-
 281 physical spikes in initial surface geometry (Zhao et al., 2018). The transient simulation
 282 period here is 0.5 yr with a timestep of 0.01 yr.

284 3.2.4 Inversion and Improvement for Basal Friction Coefficient

285 Taking the results from the surface relaxation as our ice geometry we use an inverse

286 model to retrieve the basal friction coefficient, the deviatoric stress field and ice velocity
 287 field. The inverse model adjusts the basal friction coefficient C to minimize the value
 288 of the cost function (Morlighem et al., 2010), which is defined as the difference between
 289 the simulated surface velocity and the observed,

$$290 \quad J_0 = \int_{\Gamma_s} \frac{1}{2} (|\vec{u}| - |\vec{u}_{obs}|)^2 d\Gamma \quad (6)$$

291 where Γ_s is the ice surface, \vec{u} and \vec{u}_{obs} are the simulated and observed surface velocities.

292

293 To avoid over-fitting of the inversion solution to non-physical noise in the observations,
 294 a regularization term,

$$295 \quad J_{reg} = \frac{1}{2} \int_{\Gamma_s} \left(\left(\frac{\partial C}{\partial x} \right)^2 + \left(\frac{\partial C}{\partial y} \right)^2 \right) d\Gamma, \quad (7)$$

296 is added to the cost function, then the total cost function is defined as,

$$297 \quad J_{tot} = J_0 + \lambda J_{reg}, \quad (8)$$

298 where λ is a positive regularization weighting parameter. An L-curve analysis (Hansen
 299 and Johnston, 2000) has been done for inversions to find the optimal λ by plotting the
 300 term J_{reg} as the function of J_0 . The optimal value of 10^{10} is chosen for λ to minimize J_0 .

301

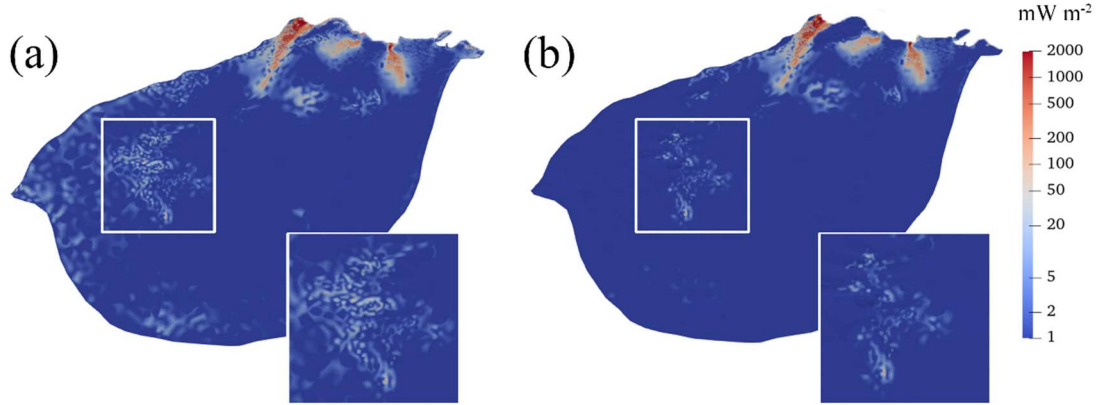
302 Basal friction in reality depends on basal temperature, i.e., it is relatively large on cold
 303 beds since the ice is frozen, and small on warm bed where basal temperature reaches
 304 pressure-melting point allowing the ice to slide (Greve and Blatter, 2009). However, in
 305 the inverse model, basal friction coefficient (Eq 5) is adjusted to match velocity
 306 observations without regard to basal temperature, which leads to unrealistic noise
 307 manifested as local spikes in modelled basal friction heat (Fig. 5a).

308

309 We improve the parameterization of β via C in Eq 5 (Section 3.2.2) by considering
 310 basal temperature T_{bed} ,

$$311 \quad \beta_{new} = \beta_{old} + \alpha(T_M - T_{bed}), \quad (9)$$

312 where β_{old} is that from by the inverse model, α is a positive factor to be tuned, T_M is
 313 pressure-dependent melting temperature. β_{new} equals β_{old} at a bed with temperate ice,
 314 and is larger than β_{old} at a bed with ice temperature lower than T_M . We tune α in the
 315 range of $[0.1, 2]$ with an interval of 0.1, and find the local spikes in modelled friction
 316 heat become fewer (Fig. 5) as α increases from 0.1 to 1, but stay almost constant with
 317 α from 1 to 2. Therefore, we take α to be 1, and use the parameterization of β_{new} in Eq
 318 5 in all the simulations. Using Eq 9, the difference of simulated and observed surface
 319 velocity is unchanged over the region except for some parts of the inland boundary.



320

321 Fig. 5. Comparison of modelled basal friction heat with basal friction coefficient β_{old} (a) and β_{new}
 322 with $\alpha=1$ (b). The white square is enlarged.

323

324 3.2.5 Basal Melt Rate

325 Based on the inverted basal velocity and basal shear stress, we can calculate the basal
 326 friction heat. We then produce the basal melt rate using the thermal equilibrium as
 327 follows (Greve and Blatter, 2009):

$$328 \quad M = \frac{G + \bar{u}_b \bar{\tau}_b + k(T) \frac{dT}{dz}}{\rho_i L}, \quad (10)$$

329 where M is the basal melt rate, G is GHF, $\bar{u}_b \bar{\tau}_b$ is the basal friction heat, $-k(T) \frac{dT}{dz}$ is

330 the upward heat conduction, ρ_i is the ice density, and L is latent heat of ice melt. The

331 ice-bed interface gets heat through GHF and friction heat but loses heat from upward
 332 heat conduction.

333 3.3 Experimental Design of coupled simulations

334 We design the coupled simulations in an 8-step scheme for coupling the forward model
 335 and inverse model similar as Zhao et al. (2018):

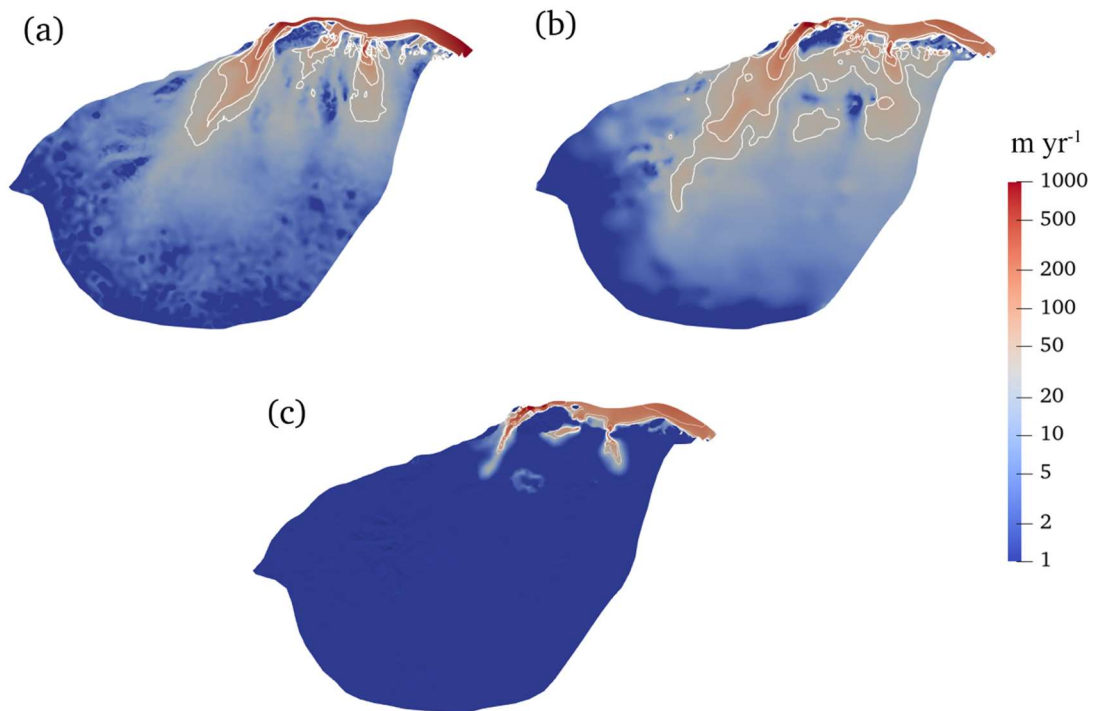
- 336 1. We run the forward model with the velocity direction taken from a mixture of the
 337 surface gradient and surface velocity observations, and get an initial modelled
 338 englacial temperature.
- 339 2. We do surface relaxation in Elmer/Ice with the englacial temperature from step
 340 1.
- 341 3. Taking the results from step 2 as the initial state, we do an inversion in Elmer/Ice
 342 using the modeled englacial temperature from step 1, to get a modelled surface
 343 velocity best fit to the observed surface velocity. The modelled surface velocity
 344 will remove some artifacts in the observed field.
- 345 4. We run the forward model using the velocity directions derived by merging the
 346 Elmer/Ice modelled velocity, the surface gradient and the surface velocity

347 observations. We use the modelled velocity by the full-Stokes inverse model to
348 constrain the basal slip ratio, then constrain rheology and shape function in the
349 forward model. Then we get an updated modelled englacial temperature.
350 5. We run the inverse model in Elmer/Ice with the improved englacial temperature
351 from step 4, and get an updated modelled velocity.
352 6. We run the forward model again using the ratio of basal sliding to column-
353 average velocity in Elmer/Ice from step 5 to constrain the slip ratio, and get a
354 further updated basal temperature.
355 7. We run the inverse model again in Elmer/Ice with the improved englacial
356 temperature from step 6, and get an updated modelled velocity and stress.
357 8. We analyze the modelled results in step 7, calculate basal friction heat and basal
358 melt rate.
359
360 We perform the above procedure for all six sets of GHF to produce six different results
361 for the basal thermal conditions.

362 **4 Simulation Results**

363 **4.1 Ice Velocity**

364 In the inverse model, the misfit between the modeled and the observed surface velocity
365 is minimized. Therefore, we get very similar distributions of modeled surface velocity
366 field using different GHFs. Fig. 6 shows the modelled velocity in the experiment using
367 Martos et al. (2017) GHF as an example. The modeled surface velocity shows spatial
368 similarities to the observed surface velocity (Fig. 6a, b). Three fast-flowing outlet
369 glaciers (Lambert Glacier, Lepekhin Glacier and Kronshtadtskiy Glacier) deliver ice to
370 the ice shelf. The velocity of the Lambert glacier exceeds 800 m yr^{-1} at the grounding
371 line. The Lepekhin Glacier and the Kronshtadtskiy Glacier have maximum flow
372 velocities of about 200 and 400 m yr^{-1} at their grounding lines, respectively. Regions
373 with large differences between modeled and observed surface velocity occupy a small
374 fraction of the whole area (Fig. 6c) and are associated with high velocity gradients. Ice
375 velocity decreases with depth. Fig. 6c shows modeled basal ice velocity. The maximum
376 basal velocity on Lambert Glacier exceeds 500 m yr^{-1} near the grounding line, and
377 maximum basal velocities on Lepekhin Glacier and the Kronshtadtskiy Glacier reach
378 about 150 and 200 m yr^{-1} at the grounding line.



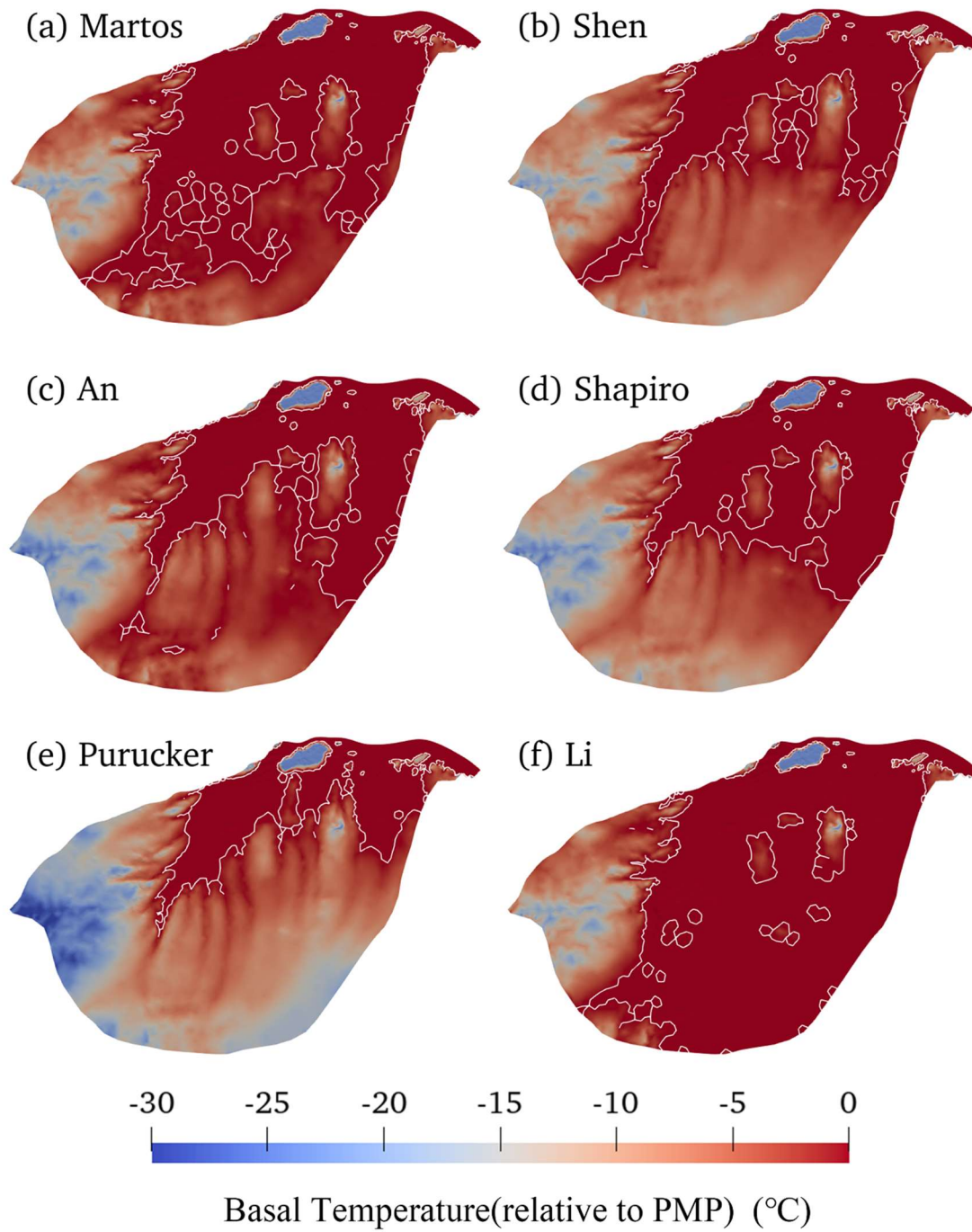
379

380 Fig. 6. (a) Observed surface velocity, (b) modeled surface velocity in the experiment using Martos
 381 et al. (2017) GHF, (c) modeled basal velocity. The white solid lines in (a), (b), and (c) represent
 382 speed contours of 30, 50, 100 and 200 m yr⁻¹, respectively. The three fast-flowing outlet glaciers in
 383 plot (a) from left to right are Lambert, Lepekhin and Kronshtadtskiy glaciers.

384

385 **4.2 Basal Ice Temperature and Heat Conduction**

386 In Fig. 7 we show the modelled basal temperature from the six experiments. The
 387 modelled ice basal temperatures in the fast-flowing regions are all at the pressure
 388 melting point (“warm”). However, there are significant differences in the modelled
 389 distribution of warm-based conditions in the slow-flowing region using different GHFs.
 390 The basal temperature is highly dependent on the GHF. In the experiment using Li et
 391 al. (2021) GHF (Fig. 7f), which has the highest GHF within the domain, the basal
 392 temperature is at the melting point over most of the domain, with extensive cold based
 393 regions confined to the southern part. The experiment using Martos et al. (2017) GHF
 394 (Fig. 7a), which has the second highest GHF, yields the second largest area of warm
 395 base, and the experiment using Purucker (2013) GHF (Fig. 7e), with the lowest GHF
 396 gives the smallest warm-based area which is concentrated around the fast-flowing ice.
 397 All experiments display cold basal temperatures to the southwest of the Lambert Glacier
 398 Basin, associated with thin ice over subglacial mountains (Fig. 1c).

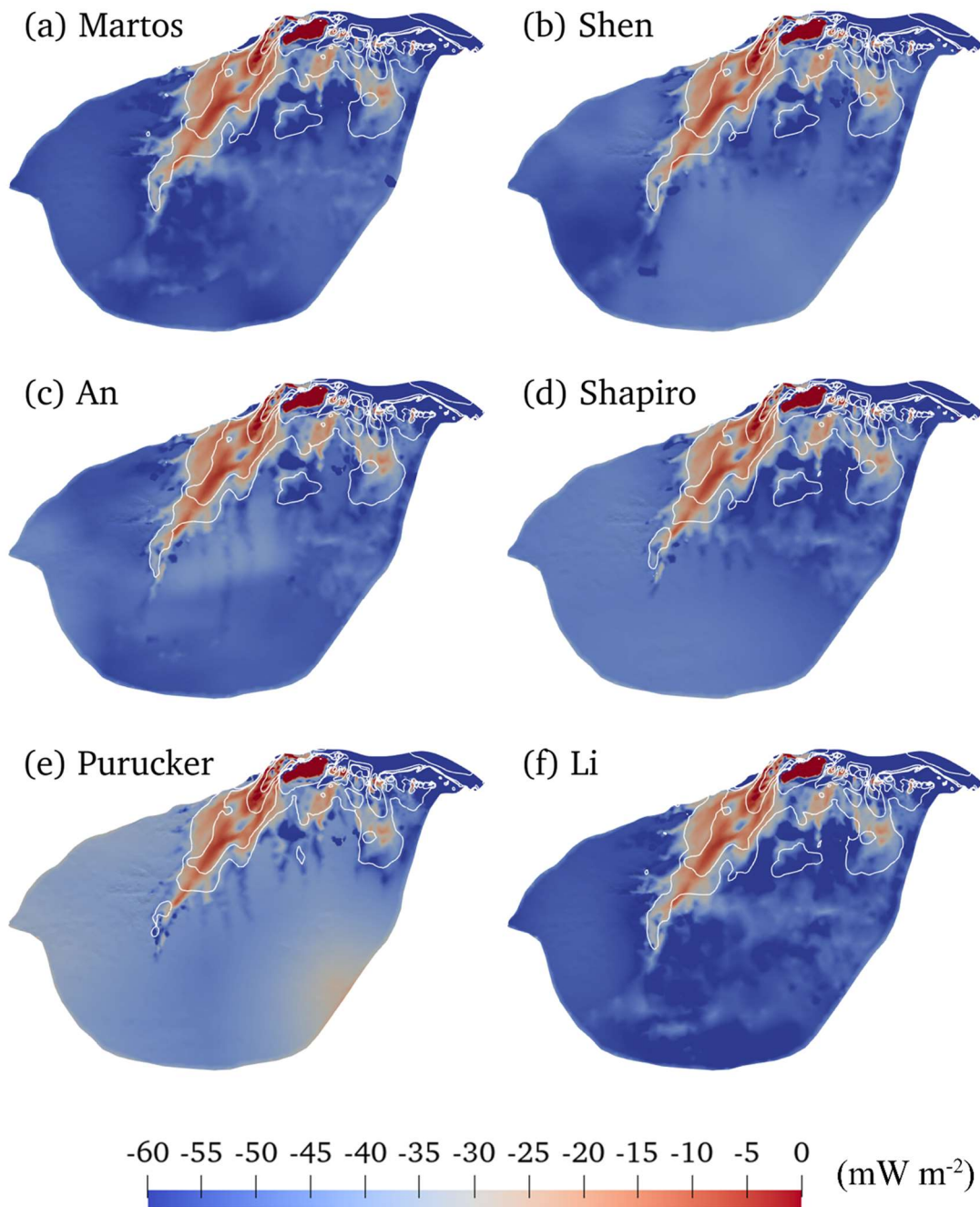


399

400 Fig. 7. Modelled basal temperature relative to pressure melting point, (a) to (f) corresponding to the

401 GHF (a) to (f) in Fig. 2. The ice bottom at the pressure-melting point is delineated by a white contour.

402



403

404 Fig. 8. Modelled heat change of basal ice by upward englacial heat conduction (unit: mW m^{-2}). The
 405 negative sign means that the upward englacial heat conduction causes heat loss from the basal ice
 406 as defined by the color bar with cooler colors representing more intense heat loss by conduction. (a)
 407 to (f) corresponding to the GHF (a) to (f) in Fig. 2. The white solid curves represent modelled speed
 408 contours of 30, 50, 100 and 200 m yr^{-1} , the same as in Fig. 6b.

409

410 Fig. 8 show the modelled heat change of basal ice by upward englacial heat conduction
 411 in the six experiments. In most regions of the fast-flowing tributaries with velocity
 412 higher than 30 m yr^{-1} , the heat loss caused by upward basal heat conduction is lower
 413 than 30 mW m^{-2} in all experiments, reflecting the development of a temperate basal

414 layer that limits the basal thermal gradient. For the vast inland areas, experiments yield
415 heat loss by upward heat conduction in the range of 45-60 mW m⁻² except for the
416 experiment driven by the Purucker (2013) GHF which has lower values around 30-45
417 mW m⁻². This is because the upward heat conduction equals GHF where basal
418 temperature is below the pressure melting point, and the Purucker (2013) GHF is lower
419 than the others.

420

421 **4.3 Basal Friction Heat**

422 There is no significant difference in modelled basal friction heat across these 6
423 experiments, reflecting the fact that all of them have been tuned to match the surface
424 velocity observations. So, we show only the modelled basal friction driven by Martos
425 et al. (2017) GHF (Fig. 5b). As expected, basal friction heat is high in fast-flowing
426 regions. The three fast-flowing tributaries have friction heat amounting to more than 50
427 mW m⁻², with the Lambert and Kronshtadtskiy glaciers having 2000 mW m⁻² at the
428 grounding line.

429

430 **4.4 Basal Melt Rate**

431 We get the basal melt rate using the thermal balance equation (Eq 10). Fig. 9 shows the
432 modelled basal melt rate in the six experiments using different GHF. Regions with basal
433 melt rate coincide with a warm base where basal temperatures reach the pressure-
434 melting point. There are significant differences in the area of basal melting among the
435 six experiments due to large variability in GHF. The experiments using Li et al. (2021)
436 and Martos et al. (2017) GHF yield the largest area with basal melting. In contrast, the
437 experiment using Purucker (2013) GHF gives the least area with basal melting (Fig.
438 10).

439

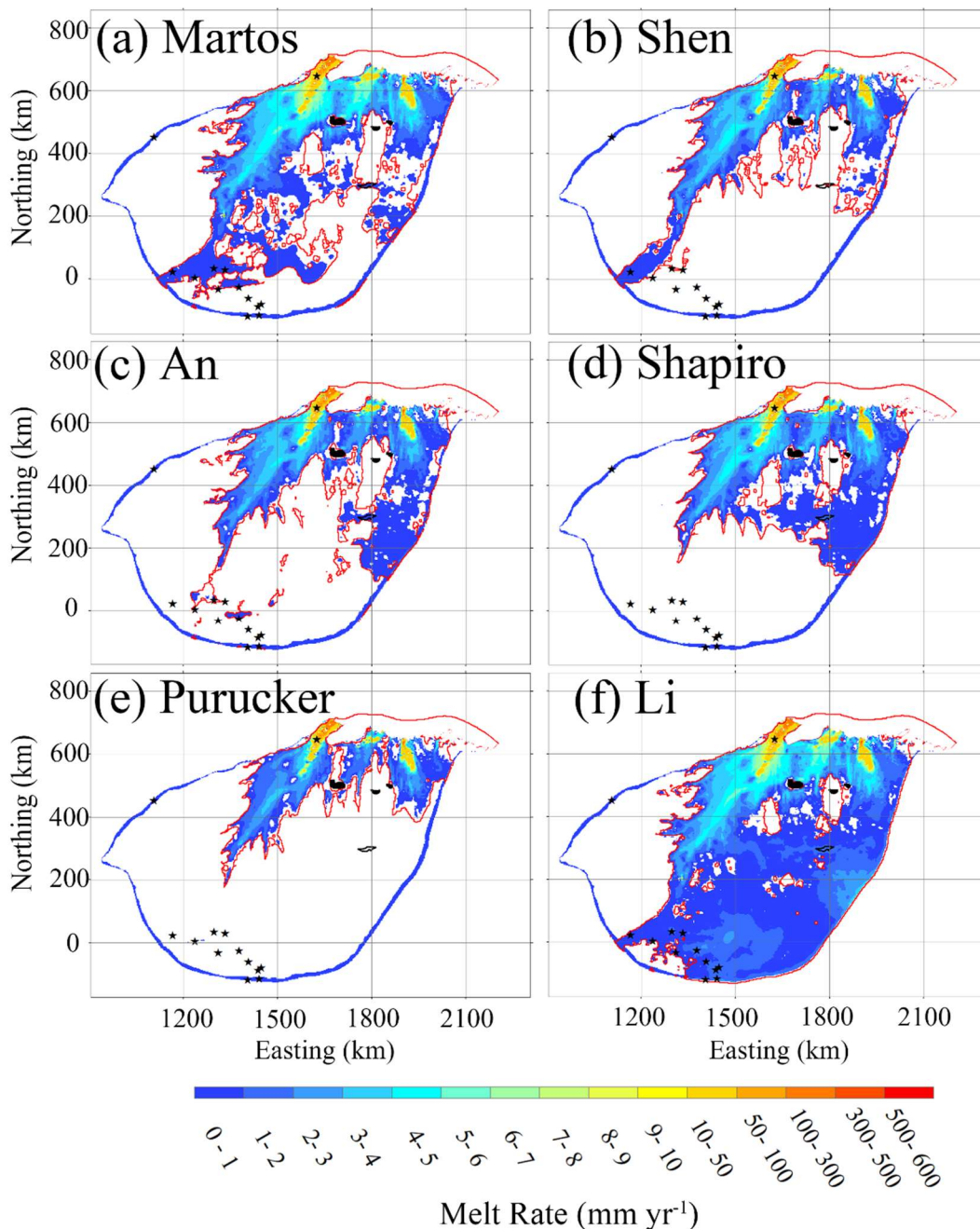
440 The modelled basal melt rate is below 5 mm yr⁻¹ in the parts of the vast inland region
441 that are warm based. Higher basal melt rates occur in fast-flowing regions (Fig. 9)
442 where frictional heat is high (Fig. 5b), despite the differences in GHF (Fig. 2). Basal
443 melt rate is above 10 mm yr⁻¹ near the grounding line, reaching 500 mm yr⁻¹ at the
444 grounding line of the central flowline running onto Amery ice shelf. Thus, in fast-
445 flowing regions, frictional heat is the dominant factor rather than GHF, consistent with
446 Larour et al. (2012) who noted that slower flowing ice in the interior of the ice sheet
447 will be more sensitive to the GHF, but frictional heat dominates GHF in regions of fast
448 ice flow.

449

450 We use the positions of observed subglacial lakes to validate simulated regions with
451 basal melting (Fig. 9). The modelled warm base in the experiment using Li et al. (2021)
452 GHF covers all the observed subglacial lakes in the domain (Fig. 9f), including the
453 recently discovered second-largest subglacial lake in Antarctica (Cui et al., 2020b). The
454 warm base in the experiment using Martos et al. (2017) GHF covers the second most
455 observed subglacial lakes (Fig. 9a), and the experiment using An et al. (2015) GHF the
456 third (Fig. 9c). The experiment using Shen et al. (2020) GHF captures two subglacial
457 lakes in the southwest of the domain (Fig. 9b), while the experiment using Shapiro and

458 Ritzwoller (2004) GHF missed many known subglacial lakes in the southwest of the
 459 domain, but successfully captures the recently discovered second-largest subglacial
 460 lake (Fig. 9b, d). The experiment using Purucker et al. (2013) GHF performs worst in
 461 recovering subglacial lake locations (Fig. 9e).

462
 463 There are localized negative values of basal melt rate, indicating basal refreezing at
 464 three locations (Fig. 9). The modelled refreezing locations are generally characterized
 465 by large gradients in ice thickness, typically thinning by 700 m across a distance of 2
 466 km. Radar surveys have not yet been done to confirm these freeze-on locations.
 467



468
 469 Fig. 9. Modelled basal melt rate (unit: mm yr^{-1}), (a) to (f) correspond to the GHF (a) to (f) in Fig. 2.
 470 The ice bottom at pressure-melting point is surrounded by a red contour. The stars denote the

471 locations of observed subglacial lakes, and the area surrounded by the black line is the likely second
472 largest subglacial lake in Antarctica. There is modelled basal refreezing at three local places painted
473 in black.

474

475 **5 Discussion**

476 Uncertainties and bias in our simulations can come from several sources. We expect
477 that the present-day accumulation rate field will be higher than the long-term average,
478 because of lower accumulation rate during glacial periods. This will tend to increase
479 the downward advection of cold ice in our model, lowering the basal temperature in
480 comparison to reality. On the other hand, we also expect that the modern-day surface
481 temperature will be higher than the long-term average temperature, again because of
482 lower temperatures during glacial periods. This will tend to increase our modeled basal
483 temperature in comparison with reality. It is unclear which of these competing biases
484 is stronger.

485

486 Subglacial topography has an influence on geothermal heat at kilometer scales.
487 Typically, it has been assumed that subglacial ridges receive less heat flow and
488 subglacial valleys receive more heat flow, in comparison to the regional average (e.g.,
489 van der Veen et al., 2007; Colgan et al., 2021). However, the effect depends on
490 subglacial rock type. Heat tends to follow the path of least resistance to the surface. The
491 thermal conductivity of rock varies with lithology, and can be either greater or smaller
492 than the thermal conductivity of ice (Willcocks & Hasterok, 2019), thus the sign of the
493 topographic effect on GHF can be either negative or positive. Without knowing a priori
494 whether the topographic effect will be positive or negative, it is hard to apply a
495 topographic correction field to the GHF input field.

496

497 GHF distribution largely governs basal thermal conditions. Many previous studies
498 (Larour et al., 2012; Pattyn, 2010; Pittard et al., 2016; Van Liefferinge and Pattyn, 2013;
499 Van Liefferinge et al. 2018) on basal temperature and basal melt have used the Shapiro
500 and Ritzwoller (2004), Fox Maule et al. (2005), Purucker (2013), and An et al. (2015)
501 GHF datasets, with few making use of the more recent Martos et al. (2017) and Li et al.
502 (2021) GHF datasets. In this study, we find that the Li et al. (2021) and Martos et al.
503 (2017) GHF datasets have higher GHF than the earlier datasets in the Lambert-Amery
504 domain and consequently have the largest area with warm base. The warmer basal
505 conditions best match the observed distribution of subglacial lakes. However, it should
506 be noted that observations of subglacial lakes are a one-sided constraint. A model result
507 that misses the observed lakes is clearly too cold at that location. But if the model result
508 shows basal melt at a place with no observed lakes, it is not clear whether this is because
509 the model is too warm, or if the subglacial water exists in a form other than ponded
510 lakes.

511

512 A lake complex beneath Devon Island ice cap in Canada exists at temperatures well
513 below pressure melting point due to large concentrations of dissolved salts (Rutishauser
514 et al., 2018), and while no similar ones are known to exist beneath the Antarctic ice

515 sheet, direct measurements of ice temperatures above water bodies are rare.
516 Furthermore, relatively high electrical conductivity beds such as water saturated clays
517 can give rise to false positives in radar detections of subglacial water bodies (Talalay et
518 al., 2020).

519
520 Our simulations make improvements on previous approaches. We use the full-Stokes
521 flow model in the inversion of basal friction field rather than a simplified physics model
522 as in Wolovick et al. (2021a). We also improve on the treatment of the basal friction
523 field by imposing a larger basal friction where the ice bottom is colder than the pressure
524 melting point, and which increases with temperature difference from freezing point.
525 These modifications produce more physically meaningful results since we expect
526 frozen beds to have high basal friction. Hence, the basal friction field is constrained by
527 simulated temperatures in addition to producing the best fitting match of simulated and
528 observed surface velocities.

529
530 Van Liefferinge and Pattyn (2013) estimated basal temperature for the Antarctica ice
531 sheet using three GHF datasets (Fox Maule et al., 2005; Shapiro and Ritzwoller, 2004;
532 Purucker, 2013), and each of the datasets were improved by the method in Pattyn (2010).
533 Their modeled temperatures show spatial similarities to the our experiment field using
534 Purucker et al. (2013) GHF. Pittard et al. (2016) did sensitivity experiments of the
535 Lambert-Amery glacial system based on 3 GHF fields (Fox Maule et al., 2005; An et
536 al., 2015; Shapiro and Ritzwoller, 2004) using the ice dynamics model PISM, and found
537 that modelled basal temperature reached the pressure melting point only under the fast-
538 flowing ice, with maximum melting rates of 500 mm yr^{-1} at places very close to the
539 grounding line of the central flowline onto the Amery ice shelf. We also model
540 maximum basal melt at similar locations in the six GHF experiments. However, the
541 Pittard et al. (2016) region of basal melt is mainly confined to the Lambert glacier
542 tributary and matches only that of our experiment using Purucker (2013) GHF.

543
544 We analyze the contribution of GHF and frictional heat to basal melt. The basal friction
545 is a significant heat sources only under fast-flowing ice. Most GHF distributions (except
546 Martos et al., 2017 and Li et al., 2021) in the grounded ice sheet near the ice shelf are
547 homogeneous, but frictional heating in the fast-flowing ice is more than 10 times higher
548 than that in the slow-flowing ice. Thus slower flowing ice in the interior of the ice sheet
549 is more sensitive to the GHF than fast-flowing ice (Larour et al., 2012).

550
551 GHF has its largest impact on the basal melt of the inland ice sheet. There are two
552 principle ways to constrain GHF: (1) direct measurement (2) inversion by multiple
553 geophysical methods. The GHFs used in this study are based on inversion of satellite
554 or aero magnetic data and seismic tomography. Direct observations of heat flux are
555 difficult to obtain in Antarctica, and satellite data are low resolution. The most efficient
556 methods is to invert the heat flux through aerial geomagnetic observation such as for
557 the Martos and Li GHF fields. However, there are still large data gaps in remote regions,
558 especially in PEL, leaving just inversion using satellite magnetic data with a lower

559 resolution. The Li et al. (2021) field uses the latest aeromagnetic data to estimate the
560 GHF in the PEL region and this gives higher values than derived previously.

561

562 To validate the modelled basal melt, we use the locations of detected subglacial lakes.
563 There may be many other undiscovered subglacial lakes beneath the study area, and
564 further discoveries would help us validate the model results, and possibly refine GHF
565 maps. In addition, further observational constraints with a two-sided sensitivity to ice
566 temperature, such as observations of subglacial freeze-on or measurements of englacial
567 attenuation, would help us to identify areas in which the GHF maps are too warm, in
568 addition to those areas in which they are too cold.

569

570 **6 Conclusions**

571 In this paper, we estimate the basal thermal conditions of the Lambert-Amery system
572 by coupling a forward model and an inverse model, based on six different GHF datasets.
573 We analyze the contribution of GHF, heat conduction, and basal friction to the modelled
574 basal melt rate. We verify the result using the locations of all known subglacial lakes,
575 and evaluate the reliability of six GHF datasets in our study domain.

576

577 Our approach is distinct from that used to find GHF fields employed by Wolovick et al.
578 (2021a), in particular the use of a full Stokes model allows the method to be extended
579 to fast flowing ice streams and ice shelf domains where neither the shallow ice nor
580 shallow shelf-approximations are valid. We also improve the basal friction calculation
581 to include information on the basal ice temperature relative to its pressure melting point.
582 This procedure results in removal of unrealistic noise manifested as local spikes in
583 modelled basal friction heat.

584

585 We find significant differences in the spatial extent of temperate ice in the slow flowing
586 areas among the six experiments due to large variability in GHF. The experiments using
587 Li et al. (2021) and the Martos et al. (2017) GHF yield the largest area with basal
588 melting, and match the subglacial lake locations best. In contrast, the experiments using
589 Purucker (2013) GHF gives the least area with basal melting and the worst match with
590 subglacial lakes locations. We suggest GHF datasets from Li et al. (2021) and Martos
591 et al. (2017) as the most suitable choice for this study region. We cannot make our own
592 GHF map from our analysis since while we can pick the GHF in places where the Li
593 and Martos geothermal heat flow maps are consistent and both agree with the
594 observations, we do not know which (if either) are correct where the Li and Martos
595 GHF datasets disagree and there are no observations. In order to make this
596 determination we would need additional observational constraints on the basal thermal
597 state, such as measured basal temperatures from deep ice cores, or observed refreeze-
598 on, but neither are available in the region.

599

600 The fast flowing region has smaller modelled basal friction coefficients, and faster basal
601 velocities, but there are large differences in basal melting rates between the 6 GHF
602 datasets. The fast-flowing tributaries have frictional heating in the range of 50-2000

603 mW m⁻². In the vast inland areas, our experiments generally yield high upward heat
604 conduction in the range of 45-60 mW m⁻² which means that GHF dominates the heat
605 content of the basal ice in the slow flow regions. The modelled basal melt rate reaches
606 50-500 mm yr⁻¹ locally in three very fast flow tributaries (Lambert, Lepekhin and
607 Kronshtadtskiy glaciers) feeding the Amery ice shelf, and is in the range of 0-5 mm yr⁻¹
608 in the inland region.

609

610 **Data availability**

611 All data sets used are publicly available.

612

613 **Acknowledgments**

614 This work was supported by the National Natural Science Foundation of China (No.
615 41941006) and National Key Research and Development Program of China
616 (2021YFB3900105).

617

618 **References**

- 619 An, M., Wiens, D. A., Zhao, Y., Feng, M., Nyblade, A. A., Kanao, M., et al.:
620 Temperature, lithosphere-asthenosphere boundary, and heat flux beneath the
621 Antarctic Plate inferred from seismic velocities, *J. Geophys. Res.: Solid Earth*, 120,
622 359-383, <https://doi.org/10.1002/2014jb011332>, 2015.
- 623 Arthern, R. J., Winebrenner, D. P., & Vaughan, D. G. Antarctic snow accumulation
624 mapped using polarization of 4.3-cm wavelength microwave emission. *Journal of*
625 *Geophysical Research: Atmospheres*, 111(D6), 2006,
626 D06107. <https://doi.org/10.1029/2004JD005667>
- 627 Budd, W. F., Warner, R. C., Jacka, T., Li, J., and Treverrow, A.: Ice flow relations for
628 stress and strain-rate components from combined shear and compression laboratory
629 experiments, *J. Glaciol.*, 59, 374-392, <https://doi.org/10.3189/2013JoG12J106>, 2013.
- 630 Colgan, W., MacGregor, J. A., Mankoff, K. D., Haagenson, R., Rajaram, H., Martos, Y.
631 M., et al. (2021). Topographic correction of geothermal heat flux in Greenland and
632 Antarctica. *Journal of Geophysical Research: Earth Surface*, 126, e2020JF005598.
633 <https://doi.org/10.1029/2020JF005598>
- 634 Cuffey, K. M., and Paterson, W. S. B.: *The physics of glaciers*, fourth edition, Elsevier,
635 Burlington, 2010.
- 636 Cui, X., Jeofry, H., Greenbaum, J. S., Guo, J., Li, L., Lindzey, L. E., et al.: Bed
637 topography of Princess Elizabeth Land in East Antarctica, *Earth Syst. Sci. Data*, 12,
638 2765-2774, <https://doi.org/10.5194/essd-2020-126>, 2020a.
- 639 Cui, X., Lang, S., Guo, J., and Sun, B.: Detecting and Searching for subglacial lakes
640 through airborne radio-echo sounding in Princess Elizabeth Land (PEL), Antarctica,
641 *E3S Web of Conferences*, 163, <https://doi.org/10.1051/e3sconf/202016304002>,
642 2020b.
- 643 Dziadek, R., Ferraccioli, F., and Gohl, K.: High geothermal heat flow beneath Thwaites
644 Glacier in West Antarctica inferred from aeromagnetic data, *Commun. Earth Environ.*,
645 2, <https://doi.org/ARTN 16210.1038/s43247-021-00242-3>, 2021.
- 646 Fox Maule, C., Purucker, M. E., Olsen, N., & Mosegaard, K. (2005). Heat flux

647 anomalies in Antarctica revealed by satellite magnetic data. *Science*, 309(5733), 464
648 – 467. <https://doi.org/10.1126/science.1106888>

649 Fretwell, P., Pritchard, H. D., Vaughan, D. G., Bamber, J. L., Barrand, N. E., Bell, R.,
650 et al.: Bedmap2: improved ice bed, surface and thickness datasets for Antarctica, *The*
651 *Cryosphere*, 7, 375–393, <https://doi.org/10.5194/tc-7-375-2013>, 2013

652 Fricker, H. A., Siegfried, M. R., Carter, S. P., and Scambos, T. A.: A decade of progress
653 in observing and modelling Antarctic subglacial water systems, *Philosophical*
654 *Transactions of the Royal Society A: Mathematical, Physical and Engineering*
655 *Sciences*, 374, 20140294, <https://doi.org/10.1098/rsta.2014.0294>, 2016.

656 Gagliardini, O., Zwinger, T., Gillet-Chaulet, F., Durand, G., Favier, L., Fleurian, B. d.,
657 et al.: Capabilities and performance of Elmer/Ice, a new-generation ice sheet model,
658 *Geosci. Model Dev.*, 6, 1299-1318, <https://doi.org/10.5194/gmd-6-1299-2013>, 2013.

659 Geuzaine, C., and Remacle, J. F.: Gmsh: A 3-D finite element mesh generator with built-
660 in pre- and post-processing facilities, *Int. J. Numer. Meth. Eng.*, 79, 1309-1331,
661 <https://doi.org/10.1002/nme.2579>, 2009.

662 Greve R, Blatter H, *Dynamics of Ice Sheets and Glaciers*, Springer, 2009.

663 Gillet-Chaulet, F., Gagliardini, O., Seddik, H., Nodet, M., Durand, G., Ritz, C., et al.:
664 Greenland ice sheet contribution to sea-level rise from a new-generation ice-sheet
665 model, *The Cryosphere*, 6, 1561-1576, <https://doi.org/10.5194/tc-6-1561-2012>, 2012.

666 Hansen, P., and Johnston, P.: Computational inverse problems in electrocardiology,
667 2000.

668 King, M. A., Coleman, R., Morgan, P. J., and Hurd, R. S.: Velocity change of the Amery
669 Ice Shelf, East Antarctica, during the period 1968–1999, *J. Geophys. Res.-Earth*, 112.
670 doi:10.1130/g37220.1, 2007.

671 Larour, E., Morlighem, M., Seroussi, H., Schiermeier, J., and Rignot, E.: Ice flow
672 sensitivity to geothermal heat flux of Pine Island Glacier, Antarctica, *J. Geophys.*
673 *Res.-Earth*, 117, <https://doi.org/10.1029/2012jf002371>, 2012.

674 Le Brocq, A. M., Payne, A. J., and Vieli, A.: An improved Antarctic dataset for high
675 resolution numerical ice sheet models (ALBMAP v1), *Earth Syst. Sci. Data*, 2, 247-
676 260, <https://doi.org/10.5194/essd-2-247-2010>, 2010.

677 Li, L., Tang, X., Guo, J., Cui, X., Xiao, E., Latif, K., et al.: Inversion of Geothermal
678 Heat Flux under the Ice Sheet of Princess Elizabeth Land, East Antarctica, *Remote*
679 *Sensing*, 13. doi:10.3390/rs13142760, 2021.

680 Martos, Y. M., Catalán, M., Jordan, T. A., Golynsky, A., Golynsky, D., Eagles, G., et al.:
681 Heat flux distribution of Antarctica unveiled, *Geophys. Res. Lett.*, 44, 11,417-
682 411,426, <https://doi.org/10.1002/2017gl075609>, 2017.

683 Maule, C. F., Purucker, M. E., Olsen, N., and Mosegaard, K.: Heat flux anomalies in
684 Antarctica revealed by satellite magnetic data, *Science*, 309, 464-467,
685 <https://doi.org/10.1126/science.1106888>, 2005.

686 Morlighem, M., Rignot, E., Binder, T., Blankenship, D., Drews, R., Eagles, G., et al.:
687 Deep glacial troughs and stabilizing ridges unveiled beneath the margins of the
688 Antarctic ice sheet, *Nat. Geosci.*, 13, 132-137, <https://doi.org/10.1038/s41561-019-0510-8>, 2020.

690 Morlighem, M., Rignot, E., Seroussi, H., Larour, E., Ben Dhia, H., and Aubry, D.:

691 Spatial patterns of basal drag inferred using control methods from a full-Stokes and
692 simpler models for Pine Island Glacier, West Antarctica, *Geophys. Res. Lett.*, 37,
693 <https://doi.org/10.1029/2010gl043853>, 2010.

694 Mouginit, J., Scheuchl, B., and Rignot, E.: MEaSURES Antarctic Boundaries for IPY
695 2007-2009 from Satellite Radar, Version 2, National Snow and Ice Data Center, 10,
696 <https://doi.org/doi.org/10.5067/AXE4121732AD>, 2017.

697 Näslund, J.-O., Jansson, P., Fastook, J. L., Johnson, J., and Andersson, L.: Detailed
698 spatially distributed geothermal heat-flow data for modeling of basal temperatures
699 and meltwater production beneath the Fennoscandian ice sheet, *Ann. Glaciol.*, 40, 95-
700 101, <https://doi.org/10.3189/172756405781813582>, 2005.

701 Pattyn, F.: Antarctic subglacial conditions inferred from a hybrid ice sheet/ice stream
702 model, *Earth Planet. Sc. Lett.*, 295, 451-461, [https://doi.org/10.1016/j.epsl.](https://doi.org/10.1016/j.epsl.2010.04.025)
703 2010.04.025, 2010.

704 Pittard, M., Roberts, J., Galton-Fenzi, B., and Watson, C.: Sensitivity of the Lambert-
705 Amery glacial system to geothermal heat flux, *Ann. Glaciol.*, 57, 56-68,
706 <https://doi.org/10.1017/aog.2016.26>, 2016.

707 Rutishauser A., Blankenship, D. D., Sharp, M., Skidmore, M. L., Greenbaum, J. S.,
708 Grima, C., Schroeder, D. M., Dowdeswell, J. A., Young, D. A., Discovery of a
709 hypersaline subglacial lake complex beneath Devon Ice Cap, Canadian Arctic, *Sci.*
710 *Adv.*2018; 4: eaar4353

711 Purucker, M. E.: Geothermal heat flux data set based on low resolution observations
712 collected by the CHAMP satellite between 2000 and 2010, and produced from the
713 MF-6 model following the technique described in Fox Maule et al. (2005), 2012.
714 Retrieved from http://webserv.cs.umt.edu/isis/index.php/Antarctica_Basal_Heat_Flux

715 Rezvanbehbahani, S., Stearns, L. A., Van der Veen, C. J., Oswald, G. K. A., and Greve,
716 R.: Constraining the geothermal heat flux in Greenland at regions of radar-detected
717 basal water, *J. Glaciol.*, 65, 1023-1034, <https://doi.org/10.1017/jog.2019.79>, 2019.

718 Rignot, E., Mouginit, J., and Scheuchl, B.: MEaSURES InSAR-based Antarctica ice
719 velocity map, version 2, Boulder, Colorado USA. NASA National Snow and Ice Data
720 Center Distributed Active Archive Center, [https://doi.org/doi.](https://doi.org/doi.org/10.5067/D7GK8F5J8M8R)
721 [org/10.5067/D7GK8F5J8M8R](https://doi.org/doi.org/10.5067/D7GK8F5J8M8R), 2017.

722 Rignot, E., Mouginit, J., Scheuchl, B., Van Den Broeke, M., Van Wessem, M. J., and
723 Morlighem, M.: Four decades of Antarctic Ice Sheet mass balance from 1979-2017,
724 *P. Natl. Acad. Sci. USA*, 116, 1095-1103, <https://doi.org/10.1073/pnas.1812883116>,
725 2019.

726 Shapiro, N. M., and Ritzwoller, M. H.: Inferring surface heat flux distributions guided
727 by a global seismic model: particular application to Antarctica, *Earth Planet. Sc. Lett.*,
728 223, 213-224, <https://doi.org/10.1016/j.epsl.2004.04.011>, 2004.

729 Shen, W., Wiens, D. A., Lloyd, A. J., and Nyblade, A. A.: A geothermal heat flux map
730 of Antarctica empirically constrained by seismic structure, *Geophys. Res. Lett.*, 47,
731 <https://doi.org/10.1029/2020gl086955>, 2020.

732 Talalay, P., Li, Y., Augustin, L., Clow, G. D., Hong, J., Lefebvre, E., Markov, A.,
733 Motoyama, H. and Ritz, C., Geothermal heat flux from measured temperature profiles
734 in deep ice boreholes in Antarctica, *The Cryosphere*, 14, 4021-4037, 2020

735 van der Veen, C. J., Leftwich, T., von Frese, R., Csatho, B. M., & Li, J. Subglacial
736 topography and geothermal heat flux: Potential interactions with drainage of the
737 Greenland ice sheet. *Geophysical Research Letters*, 34(12), 2007.

738 Van de Berg, W. J., Van den Broeke, M. R., Reijmer, C. H., & Van Meijgaard, E.
739 Characteristics of the Antarctic surface mass balance, 1958-2002, using a regional
740 atmospheric climate model. *Annals of Glaciology*, 41(1), 97-104,
741 2005. <https://doi.org/10.3189/172756405781813302>

742 Van Liefferinge, B., and Pattyn, F.: Using ice-flow models to evaluate potential sites of
743 million year-old ice in Antarctica, *Clim. Past*, 9, 2335-2345,
744 <https://doi.org/10.5194/cp-9-2335-2013>, 2013.

745 Van Liefferinge, B., Pattyn, F., Cavitte M. G. P., et al.: Promising Oldest Ice sites in East
746 Antarctica based on thermodynamical modelling. *The Cryosphere*, 12, 2773-87,
747 <https://doi.org/10.5194/tc-12-2773-2018>, 2018.

748 Willcocks, S., & Hasterok, D. Thermal refraction: Impactions for subglacial heat flux.
749 ASEG Extended Abstracts, 2019(1), 1–4. Taylor & Francis.
750 <https://doi.org/10.1080/22020586.2019.12072986>

751 Wolovick, M. J., Moore, J. C., and Zhao, L. Joint inversion for surface accumulation rate
752 and geothermal heat flow from ice-penetrating radar observations at Dome A, East
753 Antarctica. Part I: model description, data constraints, and inversion results, *J. Geophys.*
754 *Res.-Earth*, 126, 2021. <https://doi.org/10.1029/2020jf005937>, 2021a.

755 Wolovick, M. J., Moore, J. C., and Zhao, L. Joint inversion for surface accumulation rate
756 and geothermal heat flow from ice-penetrating radar observations at Dome A, East
757 Antarctica. Part II: Ice sheet state and geophysical analysis. *Journal of Geophysical*
758 *Research: Earth Surface*, 126, e2020JF005936, 2021b. <https://doi.org/10.1029/2020JF005936>

760 Wright, A., and Siegert, M.: A fourth inventory of Antarctic subglacial lakes, *Antarct.*
761 *Sci.*, 24, 659-664, <https://doi.org/10.1017/s095410201200048x>, 2012.

762 Zhao, C., Gladstone, R. M., Warner, R. C., King, M. A., Zwinger, T., and Morlighem,
763 M.: Basal friction of Fleming Glacier, Antarctica – Part 1: Sensitivity of inversion to
764 temperature and bedrock uncertainty, *The Cryosphere*, 12, 2637-2652,
765 <https://doi.org/10.5194/tc-12-2637-2018>, 2018.